

Einstein-Podolsky-Rosen Experiment with Two Bose-Einstein Condensates

Paolo Colciaghi¹,* Yifan Li¹,* Philipp Treutlein¹, and Tilman Zibold¹†*Department of Physics, University of Basel, 4056 Basel, Switzerland* (Received 9 November 2022; revised 20 February 2023; accepted 3 April 2023; published 30 May 2023)

In 1935, Einstein, Podolsky, and Rosen (EPR) conceived a gedanken experiment which became a cornerstone of quantum technology and still challenges our understanding of reality and locality today. While the experiment has been realized with small quantum systems, a demonstration of the EPR paradox with massive many-particle systems remains an important challenge, as such systems are particularly closely tied to the concept of local realism in our everyday experience and may serve as probes for new physics at the quantum-to-classical transition. In this work we report an EPR experiment with two spatially separated Bose-Einstein condensates, each containing about 700 rubidium atoms. Entanglement between the condensates results in strong correlations of their collective spins, allowing us to demonstrate the EPR paradox between them. Our results represent the first observation of the EPR paradox with spatially separated, massive many-particle systems. They show that the conflict between quantum mechanics and local realism does not disappear as the system size increases to more than a thousand massive particles. Furthermore, EPR entanglement in conjunction with individual manipulation of the two condensates on the quantum level, as we demonstrate here, constitutes an important resource for quantum metrology and information processing with many-particle systems.

DOI: [10.1103/PhysRevX.13.021031](https://doi.org/10.1103/PhysRevX.13.021031)

Subject Areas: Quantum Physics

I. INTRODUCTION

According to quantum mechanics, complementary properties of a physical system such as its position and momentum or two orthogonal components of its spin cannot be simultaneously known with arbitrary precision. This is expressed by the Heisenberg uncertainty principle [1,2], which imposes a lower bound on the product of the two uncertainties, so that better knowledge of one property necessitates greater uncertainty of the other and vice versa. This is in stark contrast to classical physics, where all properties of a system can be simultaneously known, in principle with arbitrary precision.

In their seminal work [3], Einstein, Podolsky, and Rosen (EPR) considered this aspect for a bipartite quantum system where the parts A and B are entangled through interactions. After spatially splitting the system, measurements on the two parts yield strongly correlated outcomes, which allow one to use measurements on A to predict properties of B (and vice versa). The uncertainty product of such predictions for two complementary properties of B falls below the

Heisenberg uncertainty bound of B [4]. The fact that the distant system A can be used for better predictions than what is locally possible at B revealed a conflict between quantum mechanics and the classical principle of local realism, which became known as the “EPR paradox” [5]. In a local realist world, each system possesses its properties independent of observation and independent of actions performed on spatially separated systems. In a quantum world, on the other hand, the measurements on A change the quantum state of the distant system B , a scenario Schrödinger called “steering” [5]. It was later found that not all entangled states are able to show such strong correlations [6,7]. Only a strict subset, the so-called EPR entangled states, are able to demonstrate an EPR paradox [8]. Furthermore, EPR entanglement was identified as a resource for quantum technologies such as quantum metrology, quantum teleportation, entanglement swapping, or randomness certification [9–11].

The EPR paradox has been observed with small systems of few photons or atoms, in its original form [8,12–16] or in the form of Bell tests [17–24]. How far quantum behavior extends into the macroscopic world is an open question [25], which can be addressed by performing EPR experiments with increasingly macroscopic, massive systems [8,26,27]. Generating and verifying sufficiently strong entanglement between massive many-particle systems is a challenging task, requiring excellent isolation from the environment, high-fidelity coherent manipulations, and low-noise detection. Previous experiments demonstrated

*These authors contributed equally to this work.

†tilman.zibold@unibas.ch

Published by the American Physical Society under the terms of the [Creative Commons Attribution 4.0 International license](https://creativecommons.org/licenses/by/4.0/). Further distribution of this work must maintain attribution to the author(s) and the published article's title, journal citation, and DOI.

entanglement (nonseparability) between spatially separated atomic ensembles [28,29], mechanical oscillators [30,31], and hybrid systems [32,33]. However, the observed correlations were not strong enough to demonstrate an EPR paradox.

Atomic Bose-Einstein condensates (BECs) are many-particle systems that are particularly well suited to investigate nonclassical phenomena at the quantum-to-classical boundary [34]. Being composed of neutral atoms in ultra-high vacuum, they couple very weakly to their environment and thus show excellent coherence. Furthermore, they are reliably initialized in pure states and can be manipulated and detected with high fidelity by means of radio-frequency, microwave and optical fields. Multiparticle entanglement in BECs has been demonstrated in the form of squeezed spin states [34]. These states contain EPR entanglement, which has been verified by measuring spin correlations within a single cloud of atoms using high-resolution imaging [35–38], making them a promising starting point for an EPR experiment with spatially separated systems.

In this work we observe the EPR paradox for the first time with two spatially separated, massive many-particle systems. Our experiment closely follows the original gedanken experiment in its spin variant proposed by Bohm [39,40] (see Fig. 1). We first prepare a BEC in a squeezed spin state, in which all atoms are entangled with each other. We then physically split the BEC into two distinct condensates, which can be individually

manipulated and detected on the quantum level due to their spatial separation. The two condensates inherit entanglement from the initial state, resulting in correlated measurement outcomes of their collective spins. This allows us to observe the EPR paradox between the two condensates using the criterion of Reid [4,8].

II. EXPERIMENTAL SEQUENCE

Our experiment starts by preparing a two-component ^{87}Rb BEC of approximately 1400 atoms in a static magnetic trap on an atom chip [41]. The two components refer to the internal degree of freedom: The atoms occupy the hyperfine levels $|1A\rangle \equiv |F=1, m_F=-1\rangle$ and $|2A\rangle \equiv |F=2, m_F=1\rangle$ of the electronic ground state, see Fig. 2(b), forming a collection of pseudo-spin 1/2 particles. Because of the nearly identical collisional interaction strength and magnetic moments of these states, the atoms occupy a single spatial mode. Hence, we can describe the BEC as a collective spin \hat{S} , the sum of the individual atomic pseudo-spins [34]; see Appendix A. For instance, the z component of the collective spin is given by half the population difference between the two states, $\hat{S}_z = (\hat{N}_1 - \hat{N}_2)/2$, which we can directly measure. By coherently driving the two-photon transition between $|1A\rangle$ and $|2A\rangle$ with radio frequency and microwave fields [orange in Fig. 2(b)], we are able to perform arbitrary spin rotations with high fidelity. This also allows us to measure other spin components, such as \hat{S}_x and \hat{S}_y ; see Appendix A.

We create entanglement between the atomic spins in the initial BEC through interactions, by inducing one-axis twisting dynamics [42] with a state-dependent potential on the atom chip [36,43–45]. After an interaction time of ≈ 40 ms and a subsequent spin rotation, the BEC is prepared in a squeezed spin state polarized along \hat{S}_x (i.e., $\langle \hat{S}_x \rangle \approx N/2$) with squeezed spin component \hat{S}_z [see Fig. 2(a)], whose variance is reduced by -7 dB compared to a coherent spin state [34].

We then coherently split the spin-squeezed BEC into two spatially separated, individually addressable condensates [see Fig. 2(a)]. While coherent splitting has been demonstrated in early experiments with BECs [46], the particular challenge we face here is to spatially split a two-component condensate, while maintaining nearly perfect overlap and coherence between the spin components in each of the two condensates. This is necessary so that high-fidelity coherent spin rotations can be carried out after the splitting on each condensate separately.

To split the BEC, we first release it from the trap and accelerate it with a magnetic field gradient to reduce the overall expansion time. We then coherently transfer a fraction of the atoms to states with zero magnetic moment by simultaneously driving the transitions $|1A\rangle \rightarrow |1B\rangle \equiv |F=2, m_F=0\rangle$ and $|2A\rangle \rightarrow |2B\rangle \equiv |F=1, m_F=0\rangle$ with a two-tone microwave pulse (magenta in Fig. 2). We choose

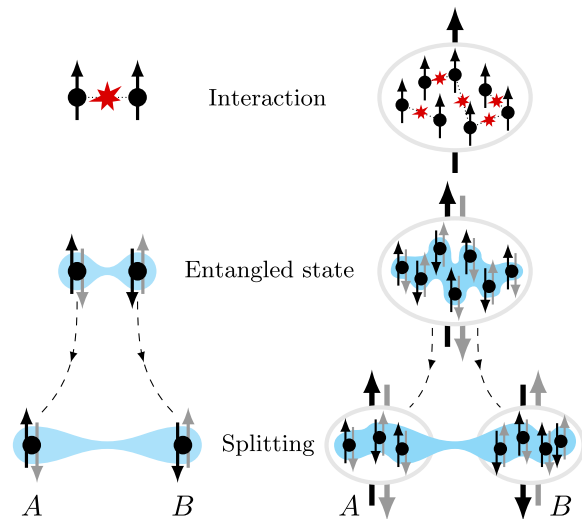


FIG. 1. Schematic of an EPR experiment with two particles (left) and with two many-particle systems (right), where the spin degree of freedom is considered [39,40]. In both cases, the particles are entangled by interactions and subsequently split into two different locations. In the case of the many-particle system, the interactions produce multipartite entanglement, which is inherited by the split systems in the form of bipartite entanglement between their collective spins.

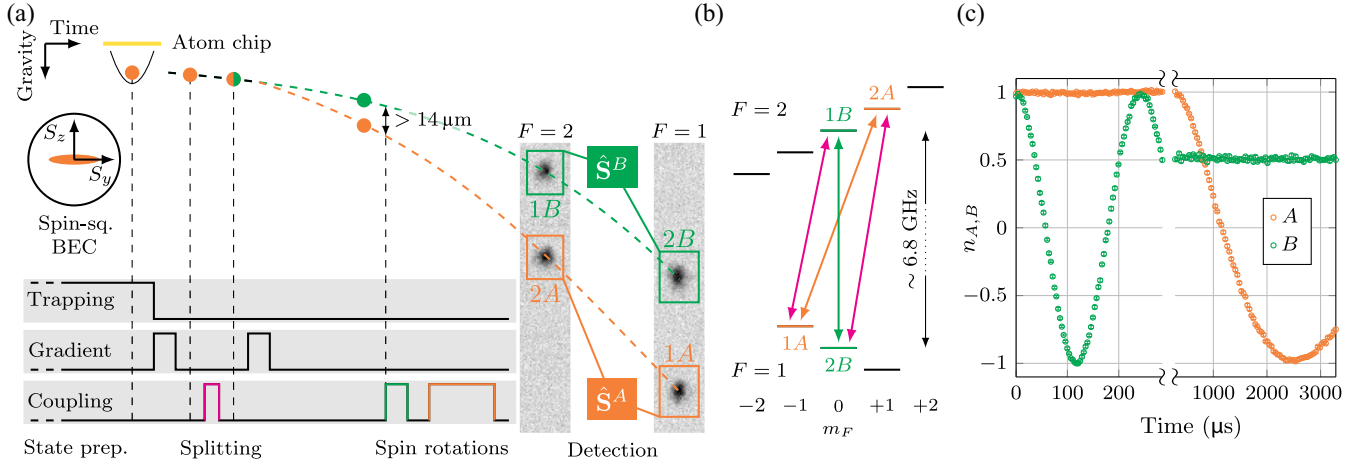


FIG. 2. Experimental sequence for spatial splitting and independent coherent control of the two condensates. (a) Space-time schematic. Orange and green color refer to condensate A and B, respectively, whereas magenta represents the splitting pulse. Bottom left: main control parameters for splitting and state manipulation. The timing is aligned with the sketch above, but not to scale. On the right, typical absorption images are shown, from which the atom numbers in all four states are determined. This corresponds to a measurement of the selected components of the collective spins \hat{S}^A and \hat{S}^B . (b) Hyperfine levels of the ^{87}Rb ground state with transitions for coherent splitting and manipulation of \hat{S}^A and \hat{S}^B . (c) Individual Rabi oscillations of the two collective spins after spatial splitting. Shown are the normalized spin components $n_{A,B} = (N_1^{A,B} - N_2^{A,B}) / (N_1^{A,B} + N_2^{A,B})$. The discontinuity in the horizontal axis denotes a change in timescale.

to transfer half of the populations (pulse duration $t_{\pi/2} \approx 70 \mu\text{s}$ for both transitions), which allows us to realize a nearly ideal 50:50 beam splitter for the atoms. A subsequent pulse of the magnetic field gradient selectively accelerates the atoms in states $|1A\rangle$ and $|2A\rangle$, spatially separating the system into two distinct two-component BECs, which we call system A (composed of states $|1A\rangle$ and $|2A\rangle$) and system B (composed of states $|1B\rangle$ and $|2B\rangle$). Since the overlap of the states in each system is preserved by the splitting mechanism, we can describe them as two collective spins \hat{S}^A and \hat{S}^B . Both transition frequencies are insensitive to magnetic field fluctuations, ensuring long coherence times [47].

Once the two condensates are split, we can coherently drive the transitions $|1A\rangle \leftrightarrow |2A\rangle$ and $|1B\rangle \leftrightarrow |2B\rangle$ with distinct radio-frequency and microwave signals, which allows us to perform arbitrary spin rotations on \hat{S}^A and \hat{S}^B independently—as demonstrated by the individual Rabi oscillations shown in Fig. 2(c). Subsequently, projective measurements of both collective spins are carried out by resonant absorption imaging: The atoms in states with $F = 2$ ($|2A\rangle$ and $|1B\rangle$) are detected on a first image by a resonant laser pulse. On a second image we detect atoms with $F = 1$ ($|1A\rangle$ and $|2B\rangle$), after they have been optically pumped to $F = 2$. Because of the large separation between the two BECs ($\approx 80 \mu\text{m}$ at the time of the first image and $\approx 100 \mu\text{m}$ at the time of the second), we can count the atoms present in all four states separately and thus obtain a measurement of the spin components $\hat{S}_z^A = (\hat{N}_1^A - \hat{N}_2^A)/2$ and $\hat{S}_z^B = (\hat{N}_1^B - \hat{N}_2^B)/2$ [see Fig. 2(a)]. Other spin components can be

measured by coherently rotating the collective spins before detection; see Appendix A.

III. EPR CRITERIA

According to quantum mechanics, \hat{S}^B satisfies the Heisenberg uncertainty relation $\mathcal{E}_{\text{Hei}}^B \equiv 4 \text{Var}(\hat{S}_z^B) \text{Var}(\hat{S}_y^B) / |\langle \hat{S}_x^B \rangle|^2 \geq 1$, which places a lower bound on the uncertainty product of \hat{S}_z^B and \hat{S}_y^B . It follows from the spin commutation relations and applies to repeated measurements on identically prepared systems. A similar relation holds for \hat{S}^A . However, if the two spins are entangled, their measurement outcomes are correlated, allowing us to use measurement outcomes obtained on \hat{S}^A to predict those obtained on \hat{S}^B . The accuracy of this prediction is quantified by the inferred variances $\text{Var}_{\text{inf}}(\hat{S}_{z,y}^B) \equiv \text{Var}(\hat{S}_{z,y}^B - \hat{S}_{z,y}^{B,\text{inf}})$, which involve linear estimates $\hat{S}_{z,y}^{B,\text{inf}} \equiv -g_{z,y} \hat{S}_{z,y}^A + c_{z,y}$ of $\hat{S}_{z,y}^B$ using $\hat{S}_{z,y}^A$. Here, $g_{z,y}$ and $c_{z,y}$ are real numbers that can be chosen to optimize the prediction, i.e., to ensure that $\langle \hat{S}_{z,y}^{B,\text{inf}} \rangle = \langle \hat{S}_{z,y}^B \rangle$ and to minimize the inferred variances.

The EPR paradox is demonstrated if the product of the inferred variances of two noncommuting spin components is lower than the associated Heisenberg uncertainty bound [4,8], that is, if the inequality

$$\mathcal{E}_{\text{EPR}}^{A \rightarrow B} \equiv \frac{4 \text{Var}_{\text{inf}}(\hat{S}_z^B) \text{Var}_{\text{inf}}(\hat{S}_y^B)}{|\langle \hat{S}_x^B \rangle|^2} \geq 1 \quad (1)$$

is violated. Observing a violation of Eq. (1) challenges our classical notions of locality and reality: it implies that an

experimenter with access to a spatially separated system \hat{S}^A can make better predictions about \hat{S}^B than what is possible if one has full local control over \hat{S}^B alone.

A related but weaker criterion exists for entanglement (nonseparability) [48]: Two spins \hat{S}^A and \hat{S}^B are in an entangled state if the inequality

$$\mathcal{E}_{\text{ent}} \equiv \frac{4 \text{Var}(g_z \hat{S}_z^A + \hat{S}_z^B) \text{Var}(g_y \hat{S}_y^A + \hat{S}_y^B)}{(|g_z g_y| |\langle \hat{S}_x^A \rangle| + |\langle \hat{S}_x^B \rangle|)^2} \geq 1 \quad (2)$$

is violated. $\mathcal{E}_{\text{EPR}}^{A \rightarrow B}$ is always larger than or equal to \mathcal{E}_{ent} , reflecting the fact that an observation of the EPR paradox requires stronger correlations than a demonstration of entanglement [7].

IV. OBSERVATION OF THE EPR PARADOX

To evaluate these criteria, we perform measurements of either the x , y , or z spin components simultaneously on both systems, repeating the experiment many times with identical preparation. The measurement basis is selected by rotating the two collective spins individually when they are completely separated, at a distance of more than 14 μm ; see Fig. 2(a). While this distance does not ensure spacelike separation between the measurements, there are no known interactions between the two condensates that could couple the collective spins across this distance on the timescale of the experiment. The outcome of every measurement of $\hat{S}_y^{A,B}$ or $\hat{S}_z^{A,B}$ (≈ 1600 repetitions each) is represented by a point in the correlation plots of Fig. 3. Strong correlations are visible between A and B in both spin components. The inference corresponds to an affine transformation (e.g.,

$S_z^B \mapsto S_z^B + g_z S_z^A - c_z$), which reduces the variance, as can be seen from the marginal histograms and 2σ intervals of the raw data (blue) and the transformed quantities (red). Splitting a squeezed spin state with a beam-splitter-like process retains part of the reduced (increased) fluctuations in the squeezed (antisqueezed) component. This can be seen from the comparison of the variance ellipse of a separable coherent spin state with the same atom number (yellow lines in Fig. 3) to the covariance ellipse of the data (blue).

The measurements of $\langle \hat{S}_x^{A,B} \rangle$ quantify the lengths of the collective spins $\hat{S}^{A,B}$ and thus determine the Heisenberg uncertainty bounds. Their values normalized to half the atom numbers correspond to the interferometric contrasts, $2|\langle \hat{S}_x^{A,B} \rangle| / \langle \hat{N}^{A,B} \rangle$, which are measures of the overall coherence of the process. We obtain 96% contrast for both \hat{S}^A and \hat{S}^B , comparable to the contrast we measure without splitting the condensate, indicating that the reduction is mostly due to spin squeezing [49] and imperfections in the initial state preparation, not due to the splitting process.

Combining all measurements we obtain

$$\mathcal{E}_{\text{EPR}}^{A \rightarrow B} = 0.81 \pm 0.03,$$

$$\mathcal{E}_{\text{EPR}}^{B \rightarrow A} = 0.77 \pm 0.03,$$

$$\mathcal{E}_{\text{ent}} = 0.35 \pm 0.02,$$

$$\mathcal{E}_{\text{Hei}}^B = 10.2 \pm 0.4,$$

$$\mathcal{E}_{\text{Hei}}^A = 9.2 \pm 0.5,$$

demonstrating both entanglement and the EPR paradox between the condensates A and B . The Heisenberg uncertainty products $\mathcal{E}_{\text{Hei}}^A$ and $\mathcal{E}_{\text{Hei}}^B$ are larger than unity due to

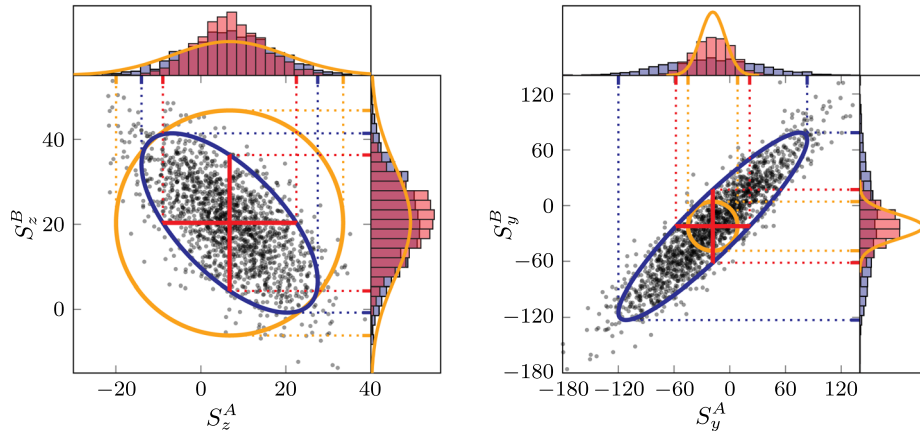


FIG. 3. Spin correlations between the two BECs and illustration of the inference mechanism. The gray dots are individual data points of simultaneous measurements of spin components S_z^A and S_z^B (left plot) and S_y^A and S_y^B (right plot) of the two systems. Data points for S_y^B are corrected for the phase shift due to the measured trigger jitter of the microwave generator (Appendix E). The blue histograms are their marginal distributions, 2σ intervals are indicated by blue dotted lines. The correlations of measurement results (2σ covariance ellipses in blue) allow one to infer measurement results of one system from the other. This reduces the variance of the prediction as shown by the histograms and the reduced 2σ intervals in red. For comparison, the 2σ variance ellipses of ideal nonentangled states with the same number of atoms are shown in yellow.

technical noise. The EPR criteria are much smaller due to the variance reduction by inferring. The variances of $\hat{S}_y^{A,B}$ are reduced by a factor of 7 and those of $\hat{S}_z^{A,B}$ by 1.7. We note that all criteria are determined without subtraction of any technical noise and that we observe the paradox both ways, inferring from $A \rightarrow B$ and from $B \rightarrow A$.

V. INDIVIDUAL CONTROL OF THE BECs

Although we rotate \hat{S}_A and \hat{S}_B individually, the results presented so far are obtained by measuring the two spins in the same bases. Since many applications of EPR entanglement require performing different measurements on the two systems, we demonstrate that our experiment is able to maintain the entanglement between \hat{S}_A and \hat{S}_B in this process. Figure 4 shows the results of measurements in which \hat{S}_B is rotated by an angle θ around the x axis with respect to \hat{S}_A , as sketched in the inset on the top left. The case $\theta = 0$ (leftmost points in Fig. 4) corresponds to the same configuration as above, i.e., simultaneous measurements of the same spin component. As θ increases, the correlations decrease and almost completely vanish for $\theta = \pi/2$, where orthogonal spin components are measured on the two condensates. This can be directly seen in the correlation plots at the bottom of Fig. 4. For $\theta = \pi$ the correlations reappear, but with opposite sign, since the spin components are now antialigned. The parameters \mathcal{E}_{ent} and $\mathcal{E}_{\text{EPR}}^{B \rightarrow A}$ fall again below unity, demonstrating that the manipulation preserves the quantum correlations.

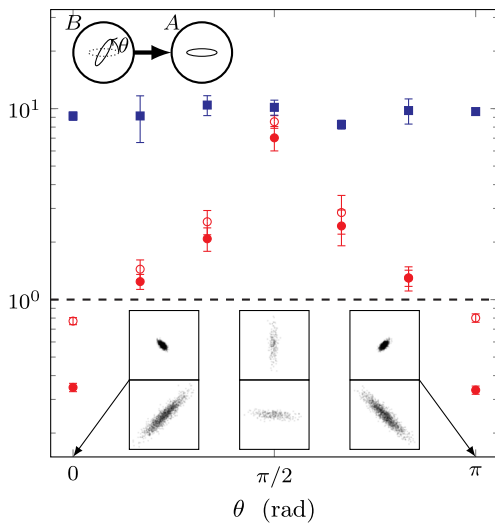


FIG. 4. Individual manipulation of the two entangled BECs on the quantum level. \hat{S}_B is rotated by an angle θ around the x axis with respect to \hat{S}_A , as sketched in the inset on the top left. The red filled circles represent \mathcal{E}_{ent} , red empty circles $\mathcal{E}_{\text{EPR}}^{B \rightarrow A}$, and blue squares $\mathcal{E}_{\text{Hei}}^A$. The EPR paradox (entanglement) is observed if $\mathcal{E}_{\text{EPR}}^{B \rightarrow A}$ (\mathcal{E}_{ent}) falls below the dashed line at unity. The insets at the bottom show the spin correlations similar to Fig. 3, with \hat{S}_z on top and \hat{S}_y at the bottom, for $\theta = 0, \pi/2$ and π .

In the setting $\theta = \pi/2$ our experiment realizes a situation discussed by Schrödinger [50], where the values of two complementary properties of system A are apparently obtained in a single experimental run: one (\hat{S}_z^A) by direct measurement on A and the other (\hat{S}_y^A) by exploiting the strong correlations to infer its value from the simultaneous measurement on B . Under the local realist assumptions that measurements reveal preexisting properties of a system and that simultaneous measurements on spatially separated systems do not disturb each other, the restrictions imposed by the Heisenberg uncertainty relation could thus be overcome [50]. Today, however, we know that local realism is inconsistent with the results of increasingly rigorous experimental tests of Bell inequalities [17–19,21–24]. In the spirit of Peres’s statement that “unperformed experiments have no results” [51], we should thus consider refraining from inferring a value for \hat{S}_y^A if it is not actually measured on system A .

VI. CONCLUSIONS

Our experiment demonstrates the EPR paradox, a cornerstone of quantum physics, for the first time between two spatially separated systems with a large number of massive particles. This shows that the conflict between quantum mechanics and the classical principles of locality and realism does not disappear in systems of increasing size and complexity, at least up to the level we demonstrate here. The key to this result is the high degree of coherence of our splitting technique together with the ability to perform high-fidelity coherent rotations of the individual systems after splitting. The ability to measure the two collective spins in different bases is also an essential prerequisite for a future Bell test, which in addition requires non-Gaussian measurements or state preparation, e.g., single-atom resolving detection [52].

EPR entanglement is a valuable resource for quantum technology. The noise reduction gained from the inference in Eq. (1), quantified by the difference between the Heisenberg products and the EPR criteria, translates to a metrological enhancement that can be exploited in quantum sensing [11,53–55]. Furthermore, EPR entanglement is the resource that guarantees the efficacy of certain quantum information protocols, such as quantum teleportation, entanglement swapping, one-sided device-independent quantum key distribution, or randomness certification [8–10].

Our experiment is particularly suited for quantum metrology applications [43,44]. One can, e.g., use one of the two systems as a small sensor to probe fields and forces with high spatial resolution and the other one as a reference to reduce the quantum noise of the first system. Moreover, the experimental techniques we demonstrate here will enable entanglement-enhanced multiparameter estimation along the lines of Ref. [55], which proposes a protocol to measure field distributions with an array of individually

addressable systems originating from the splitting of a squeezed spin state, and demonstrates that the entanglement inherited from the initial state enhances the field sensitivity.

The demonstration of EPR entanglement in conjunction with the spatial separation and individual addressability of the involved systems is thus not only significant from a fundamental point of view, but also provides the necessary ingredients to exploit EPR entanglement in many-particle systems as a resource.

ACKNOWLEDGMENTS

The authors acknowledge contributions to improving the experimental apparatus by Simon Josephy and Clara Piekarsky. This work was supported by the Swiss National Science Foundation (Grant No. 197230).

APPENDIX A: COLLECTIVE SPIN OPERATORS

The collective spin operator of a collection of N two-level systems is defined as the sum of the corresponding individual pseudo-spins,

$$\hat{S}_{x,y,z} = \frac{1}{2} \sum_{i=1}^N \hat{\sigma}_{x,y,z}^{(i)}, \quad (\text{A1})$$

where $\hat{\sigma}_{x,y,z}^{(i)}$ are the Pauli matrices applied to the i th particle. Since our atoms are indistinguishable, we can treat the two states $|1\rangle$ and $|2\rangle$ as bosonic modes and make use of Schwinger's representation of angular momentum [56], i.e., express the collective spin operators in terms of their creation (\hat{a}_1^\dagger and \hat{a}_2^\dagger) and annihilation (\hat{a}_1 and \hat{a}_2) operators:

$$\hat{S}_x = \frac{\hat{a}_1^\dagger \hat{a}_2 + \hat{a}_2^\dagger \hat{a}_1}{2}, \quad (\text{A2})$$

$$\hat{S}_y = \frac{\hat{a}_1^\dagger \hat{a}_2 - \hat{a}_2^\dagger \hat{a}_1}{2i}, \quad (\text{A3})$$

$$\hat{S}_z = \frac{\hat{a}_1^\dagger \hat{a}_1 - \hat{a}_2^\dagger \hat{a}_2}{2}. \quad (\text{A4})$$

In the same way, the atom number operator of state $|i\rangle$ can be expressed as $\hat{N}_i = \hat{a}_i^\dagger \hat{a}_i$. Thus, we can rewrite the total atom number operator as $\hat{N} = \hat{a}_1^\dagger \hat{a}_1 + \hat{a}_2^\dagger \hat{a}_2$ and the z component of the collective spin as $\hat{S}_z = (\hat{N}_1 - \hat{N}_2)/2$. As opposed to Eq. (A1), Schwinger's representation is also suited to describe systems with undefined total atom number [34], such as A and B (which are resulting from a beam-splitter-like process).

As described in the main text, we measure each spin system by detecting the atom number in the two states; thus we can measure directly the z component of the collective spin. In order to measure other spin components, we

perform collective spin rotations before detection. This is achieved by resonantly driving the transition between the two states, which generates the unitary evolution,

$$\hat{U}(t, \varphi) = e^{-i\Omega t [\cos(\varphi)\hat{S}_x + \sin(\varphi)\hat{S}_y]}, \quad (\text{A5})$$

where Ω is the Rabi frequency, t is the pulse duration, and φ is the phase of the driving field. Choosing $\Omega t = \pi/2$ (i.e., a $\pi/2$ pulse) and $\varphi = 0$ results in a collective spin rotation by $\pi/2$ around the x axis, which maps \hat{S}_y onto \hat{S}_z , $\hat{U}\hat{S}_y\hat{U}^\dagger = \hat{S}_z$. Similarly, $\Omega t = \pi/2$ and $\varphi = \pi/2$ yields a $\pi/2$ rotation around the y axis, corresponding to a change of basis between x and z , $\hat{U}\hat{S}_x\hat{U}^\dagger = \hat{S}_z$. Thus, performing a $\pi/2$ pulse with phase $\varphi = 0$ ($\varphi = \pi/2$) before detecting \hat{S}_z allows us to effectively measure \hat{S}_y (\hat{S}_x).

APPENDIX B: ADDRESSABILITY AND STRENGTH OF THE TRANSITIONS

In our experiment, multiple transitions in the hyperfine-split ground state of ^{87}Rb are coupled with radio-frequency and microwave driving fields in order to coherently split and manipulate the two-component BEC. To preserve the entanglement in this process, it is essential to prevent loss from the system by spurious driving of undesired transitions. This requires a careful choice of parameters since several of the transitions involved are nearly degenerate and differ only by quadratic Zeeman shifts, which are of the same order of magnitude as the Rabi frequencies (1–10 kHz).

In the experimental sequence up until the splitting, the populated states and applied driving frequencies are such that they do not lead to any undesired couplings. However, the driving fields used for the splitting pulse and for the subsequent rotations of \hat{S}^A are close to resonance with other relevant transitions; see Fig. 5. It is possible in principle to suppress the undesired transitions by polarization selection rules, using only driving fields with the correct circular polarization. However, since the condensate is close to the metallic atom chip surface, this is challenging to attain in our experiment and we observe that the driving fields contain all polarization components. We therefore have to ensure the selectivity by careful choice of driving field frequencies and strength.

In the case of the splitting pulse [Fig. 5(a)], the desired transition $|1A\rangle \leftrightarrow |1B\rangle$ is close to resonance with $|2B\rangle \leftrightarrow |F=2, m_F=-1\rangle$ (9 kHz detuning) and the desired $|2A\rangle \leftrightarrow |2B\rangle$ with $|1B\rangle \leftrightarrow |F=1, m_F=1\rangle$ (9 kHz detuning). These additional close-to-resonant transitions can cause atoms to be transferred from system B further to states where they are lost during the application of the magnetic gradient pulse due to the different magnetic moments. This loss mechanism is mitigated by the fact that states $|1B\rangle$ and $|2B\rangle$ are initially unpopulated and become populated only during the splitting $\pi/2$ pulse.

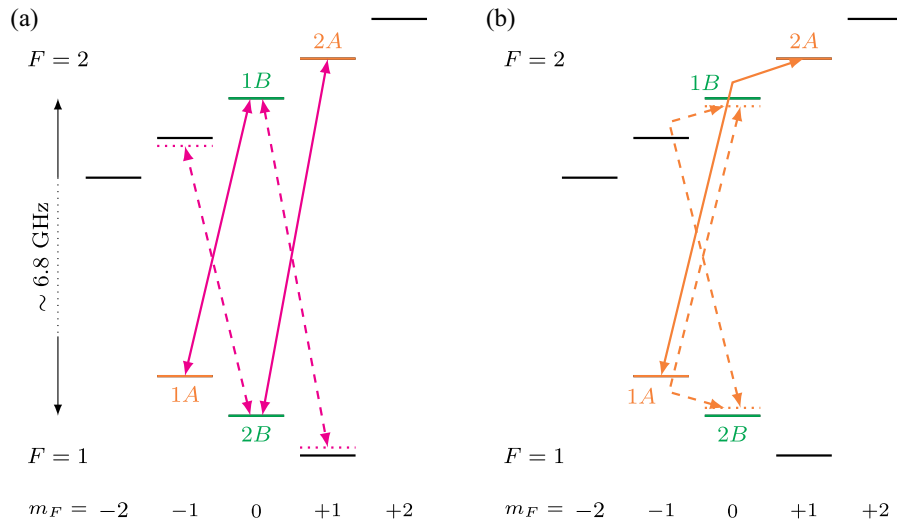


FIG. 5. Level structure of the ^{87}Rb hyperfine split ground state in the linear Zeeman regime (not to scale). The color coding is consistent with Fig. 2: orange indicates system A, green system B, and magenta the splitting transitions. The desired transitions are indicated by solid lines, the undesired close-to-resonance transitions are represented by dashed lines. (a) Transitions involved in the splitting of the condensate into systems A and B. (b) Transitions involved in driving spin rotations of $\hat{\mathbf{S}}^A$ after splitting.

In addition to this, since we only need to transfer half of the population with the splitting pulse, we can choose a detuning to make the undesired transitions further off resonant. We carefully choose a combination of detuning and small enough Rabi frequency for this pulse for which we observe no losses to the undesired states, corresponding to a detuning of 2.2 kHz and a pulse duration $t_{\pi/2}^{\text{split}} \approx 70 \mu\text{s}$.

To rotate $\hat{\mathbf{S}}^A$ after the splitting, the states $|1A\rangle$ and $|2A\rangle$ are coupled by a two-photon transition via the intermediate state $|F=2, m_F=0\rangle$ [see Fig. 5(b)]. The same driving fields are near resonance with the transition $|1B\rangle \leftrightarrow |2B\rangle$, driven as a two-photon transition with intermediate states $|F=2, m_F=-1\rangle$ and $|F=1, m_F=-1\rangle$ (10 kHz detuning). Since all transitions involved are two-photon transitions with correspondingly weak effective two-photon Rabi frequencies, this two-photon detuning can be exploited to ensure good selectivity of the pulse. The desired transition $|1A\rangle \leftrightarrow |2A\rangle$ is driven on two-photon resonance with $\pi/2$ time of $t_{\pi/2}^A \approx 960 \mu\text{s}$, ensuring that the two-photon detuning of the undesired transitions is sufficient to render spurious rotations of $\hat{\mathbf{S}}^B$ negligible.

APPENDIX C: IMAGING

We detect the atoms by resonant absorption imaging [57], which is based on comparing the shadow cast by the atoms in a resonant laser beam (absorption image) with a reference image taken without atoms. Since the criteria Eqs. (1) and (2) depend on the atom number, the accurate calibration of the imaging system is crucial. This is ensured with three types of calibration measurements. First, the conversion from absorbed light to atom number is made independent of the laser intensity following the method

described in Ref. [58]. Second, the detectivity of the four states is calibrated by ensuring that the detected total atom number is independent of the relative population in the four states when driving Rabi oscillations between them. Last, the total atom number is calibrated by observing the projection noise of a coherent spin state [59] prepared in an equal superposition of $|1A\rangle$ and $|2A\rangle$.

Since the calibration relies on projection noise measurements on equal superpositions of the involved states, it is most accurate for the measurements of \hat{S}_y and \hat{S}_z that enter the inferred variances in the EPR and entanglement criteria. In the measurements of \hat{S}_x , nearly all atoms occupy one state, and we observe a slight decrease on the order of 3% in the detected total atom number. Since we can exclude atom loss, we attribute this effect to an effective decrease in detectivity due to the increased density of the cloud. To correct for this effect, we determine $\langle \hat{S}_x^{A,B} \rangle = \langle n_x^{A,B} \rangle \langle N_{y,z}^{A,B} \rangle / 2$, i.e., we measure the relative atom number $n_x^{A,B} = (N_{1,x}^{A,B} - N_{2,x}^{A,B}) / (N_x^{A,B})$ corresponding to the interferometric contrast, and multiply by $\langle N_{y,z}^{A,B} \rangle$, the total atom number detected in the corresponding measurements along y and z.

In order to minimize detection noise, we choose the region of interest for counting atoms to be as small as possible, while still including nearly all of the atomic signal. We do this by selecting elliptical regions that include $\approx 97\%$ of the total detected atom number. To avoid any artificial noise reduction due to the small discarded signal (see the Supplemental Material of Ref. [36] for a discussion of this effect), we perform the atom number calibration after the region of interest has been determined.

Since detection noise is mainly composed of photon shot noise, we can reduce it by choosing longer imaging pulses,

as long as atomic diffusion during the imaging pulse does not increase the cloud size on the image too much. We find the lowest imaging noise for an imaging pulse duration of 70 μs . During this time, the radiation pressure accelerates the atoms, inducing a relevant Doppler shift. To maintain the resonance throughout the process, we chirp the frequency of the imaging pulses.

We use a fringe removal algorithm for optimized reference images based on linear combination of actual reference images [60]. Besides minimizing the effect of interference fringes on the reference images, this procedure further reduces the contribution of photon shot noise of the reference images.

With these optimizations the resulting photon shot noise corresponds to about ± 3 atoms in every state.

APPENDIX D: DATA ANALYSIS

To determine the EPR and entanglement criteria, we take 4500 measurements overall within 42 hours of measurement time. We subdivide the data into blocks for which we evaluate the criteria separately. Each block consists of 100 \hat{S}_z , 100 \hat{S}_y , and 20 \hat{S}_x measurements. The measurements along x are performed 10 times along the positive and negative spin directions, respectively, to reduce bias from a potential difference in the detectivity. This procedure renders the analysis robust against the effect of small, slow drifts of the experimental conditions during the many hour long measurement run, while the quantum noise of the atoms, which occurs in each shot of the experiment, is unchanged. The values of the EPR and entanglement criteria listed in the main text are the averages of the values obtained for the individual blocks. We verify that analyzing the whole dataset in one block does not change the conclusions of our paper; in this case we obtain $\mathcal{E}_{\text{EPR}}^{A \rightarrow B} = 0.87 \pm 0.04$ and $\mathcal{E}_{\text{EPR}}^{B \rightarrow A} = 0.82 \pm 0.04$.

APPENDIX E: RADIO-FREQUENCY AND MICROWAVE SIGNAL GENERATION AND LOCAL OSCILLATOR PHASE

The microwave and radio-frequency driving fields are generated with several commercial function generators. To allow phase control and simultaneous generation of the two frequencies needed for the splitting of the two-component condensate, we use an in-phase and quadrature (IQ)-modulated microwave signal (microwave generator Rohde & Schwarz SGS100A). The modulation signal is generated by a two-channel arbitrary waveform generator (Keysight 33522B). The radio-frequency signal needed for the two-photon transition of system A is generated with a separate radio-frequency source (Photonics Technologies VFG 150).

The sequence of pulses is generated by programming lists of frequencies, amplitudes, and phases that are

executed upon trigger and by gating the respective function generator signals. The digital signals used for triggering and gating are derived from a common sampling clock. All function generators are referenced to a Global-Positioning-System-disciplined 10 MHz crystal oscillator (Stanford Research Systems FS752), providing long-term frequency stability. However, absolute phase stability is not ensured since not all devices share a common sampling clock.

In a standard Ramsey experiment, a constant phase offset of the local oscillator does not matter, since the initial coupling of the two states and the final readout of the phase is done with the same local oscillator and an offset of its phase drops out. This scenario applies in our case to the spin A , composed of the states $1A$ and $2A$. The two-photon transition between these two states is driven by the microwave generator, the IQ modulator and the rf source. A constant phase offset in any of these devices will not affect the readout of the phase of spin A and thereby \hat{S}_y^A .

For spin B the situation is more complicated. The phase of system B , and thereby \hat{S}_y^B , is determined by three processes. Initially, spin B inherits the phase of spin A , which as above is determined by the phase of the microwave generator, the IQ modulator, and the rf source. The second process is the actual splitting in spin space by the two-tone microwave signal, which is generated by the microwave generator and the IQ modulator. The same devices are also generating the coupling for the last process, which is the final rotation of spin B . In contrast to spin A , the rf source appears only in the first process and therefore a phase offset of this source with respect to the other devices does not drop out in the phase sensitive measurement of \hat{S}_y^B .

Since the rf signal and the IQ modulator signal are not derived from the same sampling clock, fluctuations in the relative triggering delay of the devices by δt will lead to phase changes of $\omega_{\text{rf}} \delta t$ in system B , where $\omega_{\text{rf}} \approx 2\pi \times 1.79$ MHz. We measure typical timing fluctuations of δt on the order of 4 ns. The fluctuations are actually small when compared to the large variance observed in the measurement of \hat{S}_y^B , since this is the antisqueezed direction. However, they are relevant for the value of the much smaller inferred variance.

These fluctuations are a technical limitation that can be resolved in the future with a different setup of generators for the driving fields. In the present experiment, we correct them by directly measuring δt . We determine δt in each shot of the experiment from a measurement of the phase of the radio-frequency generator with respect to the starting time of the IQ modulator sequence with an oscilloscope. This classical information can then be used for a better estimation of $\hat{S}_y^B = \hat{S}_{y,\text{measured}}^B + g_{\delta t} \delta t$ with an optimized gain parameter $g_{\delta t}$. In Fig. 3, the data points of \hat{S}_y^B are corrected in this way. Furthermore, we use this correction in the evaluation of the EPR criterion Eq. (1). We stress that while this correction based on additional classical information can reduce classical noise, it cannot lead to a

violation of the EPR inequality, which can only be achieved by sufficiently strong entanglement between the two systems [8]. The correction based on this classical information is not applied in the evaluation of the entanglement criterion.

-
- [1] W. Heisenberg, *Über den Anschaulichen Inhalt der Quantentheoretischen Kinematik und Mechanik*, *Z. Phys.* **43**, 172 (1927).
- [2] W. Heisenberg, *Die Physikalischen Prinzipien der Quantentheorie* (S. Hirzel Verlag, Leipzig, 1930).
- [3] A. Einstein, B. Podolsky, and N. Rosen, *Can Quantum-Mechanical Description of Physical Reality Be Considered Complete?*, *Phys. Rev.* **47**, 777 (1935).
- [4] M. D. Reid, *Demonstration of the Einstein-Podolsky-Rosen Paradox Using Nondegenerate Parametric Amplification*, *Phys. Rev. A* **40**, 913 (1989).
- [5] E. Schrödinger, *Discussion of Probability Relations between Separated Systems*, *Math. Proc. Cambridge Philos. Soc.* **31**, 555 (1935).
- [6] R. F. Werner, *Quantum States with Einstein-Podolsky-Rosen Correlations Admitting a Hidden-Variable Model*, *Phys. Rev. A* **40**, 4277 (1989).
- [7] H. M. Wiseman, S. J. Jones, and A. C. Doherty, *Steering, Entanglement, Nonlocality, and the Einstein-Podolsky-Rosen Paradox*, *Phys. Rev. Lett.* **98**, 140402 (2007).
- [8] M. D. Reid, P. D. Drummond, W. P. Bowen, E. G. Cavalcanti, P. K. Lam, H. A. Bachor, U. L. Andersen, and G. Leuchs, *Colloquium: The Einstein-Podolsky-Rosen Paradox: From Concepts to Applications*, *Rev. Mod. Phys.* **81**, 1727 (2009).
- [9] D. Cavalcanti and P. Skrzypczyk, *Quantum Steering: A Review with Focus on Semidefinite Programming*, *Rep. Prog. Phys.* **80**, 024001 (2017).
- [10] R. Uola, A. C. S. Costa, H. C. Nguyen, and O. Gühne, *Quantum Steering*, *Rev. Mod. Phys.* **92**, 015001 (2020).
- [11] B. Yadin, M. Fadel, and M. Gessner, *Metrological Complementarity Reveals the Einstein-Podolsky-Rosen Paradox*, *Nat. Commun.* **12**, 2410 (2021).
- [12] C. S. Wu and I. Shakhov, *The Angular Correlation of Scattered Annihilation Radiation*, *Phys. Rev.* **77**, 136 (1950).
- [13] Z. Y. Ou, S. F. Pereira, H. J. Kimble, and K. C. Peng, *Realization of the Einstein-Podolsky-Rosen Paradox for Continuous Variables*, *Phys. Rev. Lett.* **68**, 3663 (1992).
- [14] E. Hagley, X. Maître, G. Nogues, C. Wunderlich, M. Brune, J. M. Raimond, and S. Haroche, *Generation of Einstein-Podolsky-Rosen Pairs of Atoms*, *Phys. Rev. Lett.* **79**, 1 (1997).
- [15] W. P. Bowen, R. Schnabel, P. K. Lam, and T. C. Ralph, *Experimental Investigation of Criteria for Continuous Variable Entanglement*, *Phys. Rev. Lett.* **90**, 043601 (2003).
- [16] K. V. Kheruntsyan, J.-C. Jaskula, P. Deuar, M. Bonneau, G. B. Partridge, J. Ruaudel, R. Lopes, D. Boiron, and C. I. Westbrook, *Violation of the Cauchy-Schwarz Inequality with Matter Waves*, *Phys. Rev. Lett.* **108**, 260401 (2012).
- [17] S. J. Freedman and J. F. Clauser, *Experimental Test of Local Hidden-Variable Theories*, *Phys. Rev. Lett.* **28**, 938 (1972).
- [18] M. Lamehi-Rachti and W. Mittig, *Quantum Mechanics and Hidden Variables: A Test of Bell's Inequality by the Measurement of the Spin Correlation in Low-Energy Proton-Proton Scattering*, *Phys. Rev. D* **14**, 2543 (1976).
- [19] A. Aspect, P. Grangier, and G. Roger, *Experimental Realization of Einstein-Podolsky-Rosen-Bohm Gedankenexperiment: A New Violation of Bell's Inequalities*, *Phys. Rev. Lett.* **49**, 91 (1982).
- [20] A. Aspect, J. Dalibard, and G. Roger, *Experimental Test of Bell's Inequalities Using Time-Varying Analyzers*, *Phys. Rev. Lett.* **49**, 1804 (1982).
- [21] B. Hensen, H. Bernien, A. E. Dréau, A. Reiserer, N. Kalb, M. S. Blok, J. Ruitenberg, R. F. L. Vermeulen, R. N. Schouten, C. Abellán, W. Amaya, V. Pruneri, M. W. Mitchell, M. Markham, D. J. Twitchen, D. Elkouss, S. Wehner, T. H. Taminau, and R. Hanson, *Loophole-Free Bell Inequality Violation Using Electron Spins Separated by 1.3 Kilometres*, *Nature (London)* **526**, 682 (2015).
- [22] M. Giustina, M. A. M. Versteegh, S. Wengerowsky, J. Handsteiner, A. Hochrainer, K. Phelan, F. Steinlechner, J. Kofler, J.-Å. Larsson, C. Abellán *et al.*, *Significant-Loophole-Free Test of Bell's Theorem with Entangled Photons*, *Phys. Rev. Lett.* **115**, 250401 (2015).
- [23] L. K. Shalm, E. Meyer-Scott, B. G. Christensen, P. Bierhorst, M. A. Wayne, M. J. Stevens, T. Gerrits, S. Glancy, D. R. Hamel, M. S. Allman *et al.*, *Strong Loophole-Free Test of Local Realism*, *Phys. Rev. Lett.* **115**, 250402 (2015).
- [24] W. Rosenfeld, D. Burchardt, R. Garthoff, K. Redeker, N. Ortegel, M. Rau, and H. Weinfurter, *Event-Ready Bell Test Using Entangled Atoms Simultaneously Closing Detection and Locality Loopholes*, *Phys. Rev. Lett.* **119**, 010402 (2017).
- [25] A. J. Leggett, *Testing the Limits of Quantum Mechanics: Motivation, State of Play, Prospects*, *J. Phys. Condens. Matter* **14**, R415 (2002).
- [26] A. J. Leggett, *How Far Do EPR-Bell Experiments Constrain Physical Collapse Theories?*, *J. Phys. A* **40**, 3141 (2007).
- [27] E. G. Cavalcanti and M. D. Reid, *Uncertainty Relations for the Realization of Macroscopic Quantum Superpositions and EPR Paradoxes*, *J. Mod. Opt.* **54**, 2373 (2007).
- [28] B. Julsgaard, A. Kozhekin, and E. S. Polzik, *Experimental Long-Lived Entanglement of Two Macroscopic Objects*, *Nature (London)* **413**, 400 (2001).
- [29] C. W. Chou, H. de Riedmatten, D. Felinto, S. V. Polyakov, S. J. van Enk, and H. J. Kimble, *Measurement-Induced Entanglement for Excitation Stored in Remote Atomic Ensembles*, *Nature (London)* **438**, 828 (2005).
- [30] S. Kotler, G. A. Peterson, E. Shojaei, F. Lecocq, K. Cicak, A. Kwiatkowski, S. Geller, S. Glancy, E. Knill, R. W. Simmonds, J. Aumentado, and J. D. Teufel, *Direct Observation of Deterministic Macroscopic Entanglement*, *Science* **372**, 622 (2021).
- [31] L. M. de Lépinay, C. F. Ockeloen-Korppi, M. J. Woolley, and M. A. Sillanpää, *Quantum Mechanics-Free Subsystem with Mechanical Oscillators*, *Science* **372**, 625 (2021).
- [32] M. Lettner, M. Mücke, S. Riedl, C. Vo, C. Hahn, S. Baur, J. Bochmann, S. Ritter, S. Dürr, and G. Rempe, *Remote Entanglement between a Single Atom and a Bose-Einstein Condensate*, *Phys. Rev. Lett.* **106**, 210503 (2011).

- [33] R. A. Thomas, M. Parniak, C. Østfeldt, C. B. Møller, C. Bærentsen, Y. Tsaturyan, A. Schliesser, J. Appel, E. Zeuthen, and E. S. Polzik, *Entanglement between Distant Macroscopic Mechanical and Spin Systems*, *Nat. Phys.* **17**, 228 (2021).
- [34] L. Pezzé, A. Smerzi, M. K. Oberthaler, R. Schmied, and P. Treutlein, *Quantum Metrology with Nonclassical States of Atomic Ensembles*, *Rev. Mod. Phys.* **90**, 035005 (2018).
- [35] J. Peise, I. Kruse, K. Lange, B. Lücke, L. Pezzé, J. Arlt, W. Ertmer, K. Hammerer, L. Santos, A. Smerzi, and C. Klempt, *Satisfying the Einstein-Podolsky-Rosen Criterion with Massive Particles*, *Nat. Commun.* **6**, 8984 (2015).
- [36] M. Fadel, T. Zibold, B. Décamps, and P. Treutlein, *Spatial Entanglement Patterns and Einstein-Podolsky-Rosen Steering in Bose-Einstein Condensates*, *Science* **360**, 409 (2018).
- [37] P. Kunkel, M. Prüfer, H. Strobel, D. Linnemann, A. Frölian, T. Gasenzer, M. Gärtner, and M. K. Oberthaler, *Spatially Distributed Multipartite Entanglement Enables EPR Steering of Atomic Clouds*, *Science* **360**, 413 (2018).
- [38] K. Lange, J. Peise, B. Lücke, I. Kruse, G. Vitagliano, I. Apellaniz, M. Kleinmann, G. Tóth, and C. Klempt, *Entanglement between Two Spatially Separated Atomic Modes*, *Science* **360**, 416 (2018).
- [39] D. Bohm, *Quantum Theory* (Prentice-Hall, Inc., New York, 1951).
- [40] D. Bohm and Y. Aharonov, *Discussion of Experimental Proof for the Paradox of Einstein, Rosen, and Podolsky*, *Phys. Rev.* **108**, 1070 (1957).
- [41] P. Böhi, M. F. Riedel, J. Hoffrogge, J. Reichel, T. W. Hänsch, and P. Treutlein, *Coherent Manipulation of Bose-Einstein Condensates with State-Dependent Microwave Potentials on an Atom Chip*, *Nat. Phys.* **5**, 592 (2009).
- [42] M. Kitagawa and M. Ueda, *Squeezed Spin States*, *Phys. Rev. A* **47**, 5138 (1993).
- [43] M. F. Riedel, P. Böhi, Y. Li, T. W. Hänsch, A. Sinatra, and P. Treutlein, *Atom-Chip-Based Generation of Entanglement for Quantum Metrology*, *Nature (London)* **464**, 1170 (2010).
- [44] C. F. Ockeloen, R. Schmied, M. F. Riedel, and P. Treutlein, *Quantum Metrology with a Scanning Probe Atom Interferometer*, *Phys. Rev. Lett.* **111**, 143001 (2013).
- [45] R. Schmied, J.-D. Bancal, B. Allard, M. Fadel, V. Scarani, P. Treutlein, and N. Sangouard, *Bell Correlations in a Bose-Einstein Condensate*, *Science* **352**, 441 (2016).
- [46] M. R. Andrews, C. G. Townsend, H.-J. Miesner, D. S. Durfee, D. M. Kurn, and W. Ketterle, *Observation of Interference between Two Bose Condensates*, *Science* **275**, 637 (1997).
- [47] Y. Li, K. Pawłowski, B. Décamps, P. Colciaghi, M. Fadel, P. Treutlein, and T. Zibold, *Fundamental Limit of Phase Coherence in Two-Component Bose-Einstein Condensates*, *Phys. Rev. Lett.* **125**, 123402 (2020).
- [48] V. Giovannetti, S. Mancini, D. Vitali, and P. Tombesi, *Characterizing the Entanglement of Bipartite Quantum Systems*, *Phys. Rev. A* **67**, 022320 (2003).
- [49] D. J. Wineland, J. J. Bollinger, W. M. Itano, and D. J. Heinzen, *Squeezed Atomic States and Projection Noise in Spectroscopy*, *Phys. Rev. A* **50**, 67 (1994).
- [50] E. Schrödinger, *Die Gegenwärtige Situation in der Quantenmechanik*, *Naturwissenschaften* **23**, 844 (1935).
- [51] A. Peres, *Unperformed Experiments Have No Results*, *Am. J. Phys.* **46**, 745 (1978).
- [52] E. Oudot, J.-D. Bancal, P. Sekatski, and N. Sangouard, *Bipartite Nonlocality with a Many-Body System*, *New J. Phys.* **21**, 103043 (2019).
- [53] M. Gessner, L. Pezzé, and A. Smerzi, *Sensitivity Bounds for Multiparameter Quantum Metrology*, *Phys. Rev. Lett.* **121**, 130503 (2018).
- [54] M. Fadel, B. Yadin, Y. Mao, T. Byrnes, and M. Gessner, *Multiparameter Quantum Metrology and Mode Entanglement with Spatially Split Nonclassical Spin States*, *arXiv:2201.11081*.
- [55] Y. Baamara, M. Gessner, and A. Sinatra, *Quantum-Enhanced Multiparameter Estimation and Compressed Sensing of a Field*, *SciPost Phys.* **14**, 050 (2023).
- [56] J. J. Sakurai, *Modern Quantum Mechanics* (Addison-Wesley Publishing Company, Boston, 1994).
- [57] W. Ketterle, D. S. Durfee, and D. M. Stamper-Kurn, *Making, Probing and Understanding Bose-Einstein Condensates*, <https://arxiv.org/abs/cond-mat/9904034v2>.
- [58] G. Reinaudi, T. Lahaye, Z. Wang, and D. Guéry-Odelin, *Strong Saturation Absorption Imaging of Dense Clouds of Ultracold Atoms*, *Opt. Lett.* **32**, 3143 (2007).
- [59] W. Muessel, H. Strobel, M. Joos, E. Nicklas, I. Stroescu, J. Tomkovič, D. B. Hume, and M. K. Oberthaler, *Optimized Absorption Imaging of Mesoscopic Atomic Clouds*, *Appl. Phys. B* **113**, 69 (2013).
- [60] C. F. Ockeloen, A. F. Tauschinsky, R. J. C. Spreeuw, and S. Whitlock, *Detection of Small Atom Numbers through Image Processing*, *Phys. Rev. A* **82**, 061606(R) (2010).